

FINAL 6D MUON IONIZATION COOLING USING STRONG FOCUSING QUADRUPOLES

T. L. Hart, J. G. Acosta, L. M. Cremaldi, S. J. Oliveros, and D. J. Summers
University of Mississippi, Oxford, MS 38677 USA
D. V. Neuffer, Fermilab, Batavia, IL 60510 USA

Abstract

Low emittance muon beam lines and muon colliders are potentially a rich source of BSM physics for future experimenters. A muon beam normalized emittance of $\epsilon_{x,y,z} = (280, 280, 1570)\mu\text{m}$ has been achieved in simulation with short solenoids and a betatron function of 3 cm. Here we use ICOOL and MAD-X to explore using a 400 MeV/c muon beam and strong focusing quadrupoles to achieve a normalized transverse emittance of $100\mu\text{m}$ and complete 6D cooling. The low beta regions, as low as 5 mm, produced by the quadrupoles are occupied by dense, low Z absorbers, such as lithium hydride or beryllium, that cool the beam transversely. Equilibrium transverse emittance is linearly proportional to the transverse betatron function. Reverse emittance exchange with septa and/or wedges is then used to decrease transverse emittance from 100 to $25\mu\text{m}$ at the expense of longitudinal emittance for a high energy lepton collider. Cooling challenges include chromaticity correction, momentum passband overlap, quadrupole acceptance, and staying in phase with RF.

INTRODUCTION

Ionization cooling is the only cooling technique fast enough for muons and is being tested at the MICE [1–6] experiment. The basic theory of transverse and longitudinal cooling is described in [7]. Two cooling schemes [8, 9] have been proposed to reduce muon emittances for a lepton collider [10–20]. Simulation results are shown in Table 1.

Table 1: Helical and Rectilinear Cooling Channel normalized 6D emittances ϵ_{6D} from simulations and the emittances needed for a muon collider. The channels cool by over five orders of magnitude and need less than a factor of 10 more for a collider. The 21 bunches present after initial phase rotation are also merged into one bunch during cooling [21].

	ϵ_x mm	ϵ_y mm	ϵ_z mm	ϵ_{6D} mm^3
Initial Emittance [8]	48.6	48.6	17.0	40,200
Helical Cooling [9]	0.523	0.523	1.54	0.421
Rectilinear Cooling [8]	0.28	0.28	1.57	0.123
Muon Collider [22]	0.025	0.025	70	0.044

For a given magnetic field, quadrupole focusing can achieve lower betatron functions than solenoids to reduce the equilibrium emittances below those shown in Table 1.

CHANNEL DESIGN

Low equilibrium emittance requires low $\langle \beta_{\perp} \rangle$. Strong quadrupole focusing [23, 24] can achieve β_{\perp}^* values within the required 0.5 to 2.0 cm range. A half cell is composed of four quadrupole magnets; the magnet (Q0) is a coupling quadrupole preceded by an RF (radio frequency) cavity ($L = 0.125\text{ m}$) and separated by three following RF ($L = 0.125\text{ m}$) cavities from Q1. The 650 MHz RF has a phase angle 11.5° away from zero crossing and a 27.87 MV/m gradient. The following quadrupole magnets (Q2, Q3) are separated by a short drift space to try to avoid excessive fringe field interference [25] between magnets, as shown in Fig. 1.

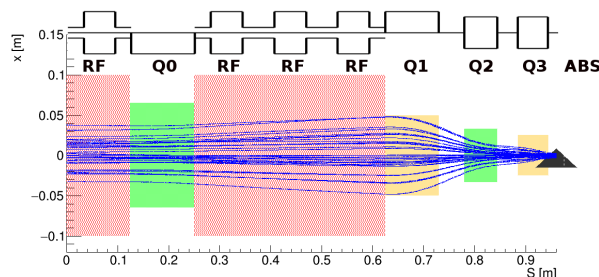


Figure 1: Half cell dimensions. Four identical RF cavities get a total of 50 cm giving a half cell length of 96 cm.

The bore diameter and length for the first quadrupole magnet Q0 is 12.5 cm. The Q0 magnet works as a coupling quadrupole reducing the betatron function maximum and allows the addition of more RF cavities to increase longitudinal synchrotron focusing. The bore diameter and length for the second quadrupole (Q1) is 10.5 cm followed by a Q2 magnet with length and diameter of 6.5 cm. A 6.0 cm long central quadrupole Q3 with 3 cm bore radius is added to reduce both the chromaticity and the minimum beta function. The 192 cm long full cell has a 3 cm drift space for an absorber. The quadrupoles Q2 and Q3 have a dipole magnetic component to produce an uniform dispersion of 4.1 mm at the absorber space [26–28].

This configuration provides strong focusing using magnetic pole tip fields of $Q0 = 0.75\text{ T}$, $Q1 = 4.69\text{ T}$, $Q2 = 9.02\text{ T}$ and $Q3 = 11.40\text{ T}$. Quadrupoles with peak fields of more than 12 T have been built with Nb_3Sn [29, 30]. The betatron function evolution for the full cell is shown in Fig. 2. The transported beam has $\beta_{x,max} \approx 2\beta_{y,max}$.

Full Cell Constraints

MAD-X [31, 32] sets magnet parameters to constrain the phase advances per 1.92 m long full cell to

1: Circular and Linear Colliders

A09 - Muon Accelerators and Neutrino Factories

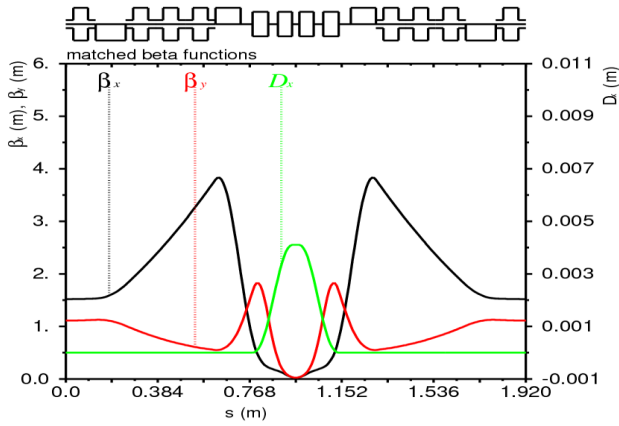


Figure 2: Full cell betatron function vs. distance s . The Courant-Snyder [33] parameters evolution through the cell are given by MAD-X.

$\mu_x, \mu_y = (0.68, 0.70)$ rad. Dispersion is flat and constant at the absorber place and zero at the cell ends. The average transverse betatron functions over the 3 cm long absorber regions is less than 3 cm for a 400 MeV/c muon.

The quadrupole doublet configuration is designed for a beam near 400 MeV/c. $\beta_x^*, \beta_y^* = (2.2, 2.7)$ cm at the centers of the absorbers. Momentum variations affect the longitudinal locations of β_x^* and β_y^* as Fig. 3 shows and can shift the minimums outside the absorbers.

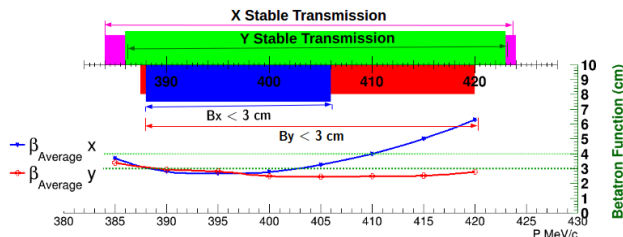


Figure 3: The pink bar is the region where the magnetic lattice has stable transmission for X, the green bar shows the stable transmission band for the Y dimension. The red and blue bars indicate that the momentum ranges where $\beta_x < 3$ cm and $\beta_y < 3$ cm are $388 < p < 402$ MeV/c and $391 < p < 422$ MeV/c, respectively.

As noted in Fig. 2 β^* is small only over a limited longitudinal distance, so the absorber must be dense and short [34]. For this configuration, the absorber is 3 cm long at the reference orbit.

Wedge for Emittance Exchange

The Q2, Q3 quadrupoles have dipole magnetic field components of 0.49 T and 0.68 T calculated to create a constant $\eta = 4.1$ mm dispersion at the absorber region as Fig. 2 shows.

A 105° lithium hydride wedge is placed at the center of the 1.92 m long full cell, as shown in Fig. 4. The ends of the wedge extend into the Q3 magnet bores on each side of the wedge. The wedge geometry and the dispersion magnitude

modify the partition numbers [7] as equation 1 shows.

$$g_L = g_{L,0} + \frac{\eta}{W}, g_x = 1 - \frac{\eta}{W} \quad (1)$$

where η is the dispersion magnitude and W the distance from wedge apex to the orbit reference center. The values for η and W are chosen to reduce the equilibrium longitudinal emittance at the expense of the equilibrium x emittance. This emittance exchange prevents severe longitudinal beam heating and results in longitudinal and transverse beam cooling.

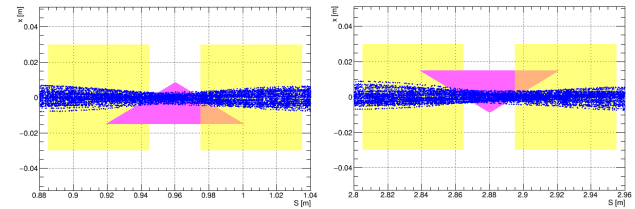


Figure 4: Wedge positions at the centers of the first and second cells.

Two consecutive cells have opposite bending directions to make a snake channel configuration.

FIRST STAGE SIMULATION

The first stage of the channel is simulated using G4beamline [35] and ICOOL [36]. The simulation runs 1000 muons with $p = 400 \pm 8$ MeV/c through 68 full cells (total length = 130.56 m) and achieves 99% beam transmission through a lattice with no RF cavities and no absorbers (magnets only). Beam transmission through the last two cells of the magnets only lattice is shown in Fig. 5.

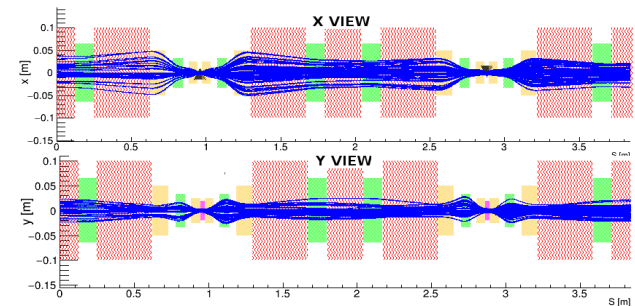


Figure 5: Beam transmission through the last 2 of 66 cells for a beam with initial transverse emittances of $\epsilon_x = 320 \mu\text{m}$ rad and $\epsilon_y = 270 \mu\text{m}$ rad. $p = 400 \pm 8$ MeV/c. The large red blocks are RF cavities, and the green and yellow blocks are quadrupoles.

When the absorbers and RF are included and the stochastic processes are on except for decays, the transmission drops to 55%. Figure 6 shows transmission vs. distance.

The first channel stage was simulated using ICOOL and G4beamline and had initial emittances of $\epsilon_{x,y,z} = (0.377, 0.246, 1.250)$ mm rad. The normalized emittances are reduced to $\epsilon_{x,y,z} = (0.250, 0.196, 0.970)$ mm rad as Fig. 7

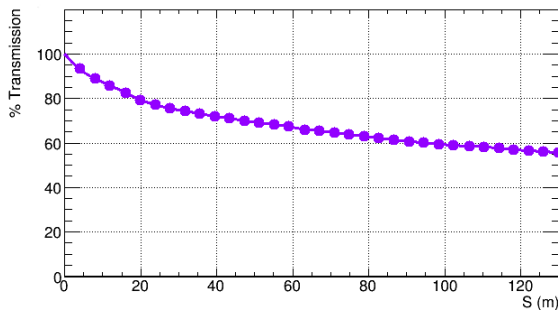


Figure 6: 55 % Transmission through a 130.56 meter long channel (68 full cells).

and Fig. 8 show. The total $\epsilon_{6D,N}$ emittance is reduced by 59% by the 130.56 meter long channel, but this reduction is a combination of beam loss through scraping and beam cooling.

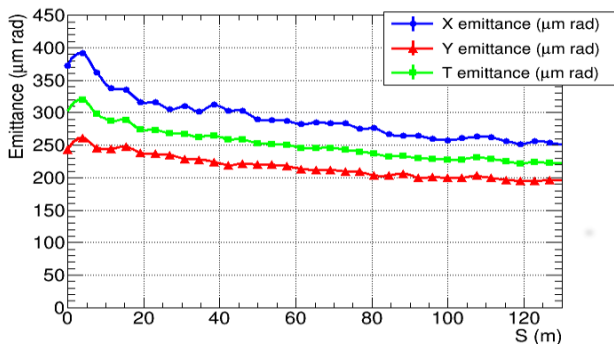


Figure 7: Transverse emittance evolution for Stage 1. The initial transverse emittance goes from $301 \mu\text{m rad}$ to $221 \mu\text{m rad}$. (Emittances are calculated using the ICOOL's eigemit tool).

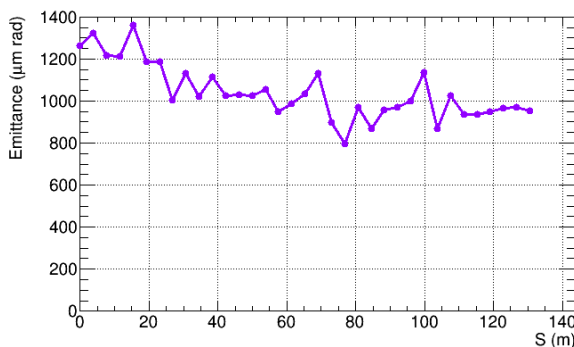


Figure 8: Longitudinal emittance evolution for Stage 1. The Z-X emittance prevents a natural longitudinal emittance increase.

Channel Stages

Calculations [24], but not simulations, have been done for more channel stages to complete the 6D cooling.

The low β_{\perp}^* regions of these additional stages are occupied by absorbers made with different low Z materials such as lithium hydride, beryllium, or diamond. Table 2 shows why diamond is being considered. In spite of the equilibrium emittance increment of a factor of two from LiH to diamond, the energy lost per centimeter increases by a factor of four. Thus, the absorber thickness can be less with the same energy loss. If β^* is reduced enough, the transverse equilibrium emittance is reduced as well, and the desired cooling can still occur.

Table 2: Material calculated equilibrium emittances. dE/ds is the energy loss at $p = 400 \text{ MeV}/c$. The equilibrium emittances are calculated for $\langle \beta_{\perp} \rangle = 2.5 \text{ cm}$, $\beta_L = 40 \text{ cm}$, wedge angle $\alpha_w = 105^\circ$ and $\Delta g = 0.356$.

Material	dE/ds MeV/cm	$g_{L,0}$ $\times 10^{-2}$	$\epsilon_{X,eq}$ $\mu\text{m}\cdot\text{rad}$	$\epsilon_{Y,eq}$ $\mu\text{m}\cdot\text{rad}$	$\epsilon_{L,eq}$ $\mu\text{m}\cdot\text{rad}$
H ₂ liquid	0.288	2.004	137.8	88.75	1626
LiH	1.622	2.648	223.2	143.8	1667
Be	3.075	3.414	324.1	208.8	1714
B ₄ C	4.334	3.836	407.6	262.5	1739
Diamond	6.474	3.712	454.9	288.8	1732

To optimize the channel length, four or five stages with different material absorbers are required. The expected emittance evolution through the channel is plotted in [24]. For 400 MeV/c muons, each channel stage length can be optimized in order to keep the total length as short as possible. Longitudinal betatron functions for dense materials are lower than 40 cm due to the smaller RF cavity voltage gradients needed to recover the lost energy. This enables the reduction of the transverse angles of muons through the stages and lower transverse emittances.

CONCLUSION

The quadrupole channel shows a factor of 2.4 6D emittance reduction with 55% (52% with decays on) transmission through the first 130.56 meters stage. Four stages may be required to reduce the 6D emittance to the required level, using various dense absorbers. The transmission needs to be improved to roughly 85% per stage. Reverse emittance exchange with septa [24, 37–39] and/or wedges [40] is then used to decrease transverse emittance from 100 to 25 μm at the expense of longitudinal emittance for a high energy lepton collider.

Many thanks to Yuri Alexahin, Scott Berg, Chandra Bhat, Alex Bogacz, Dave Cline, Mary Anne Cummings, DOE, Al Garren, Harold Kirk, Robert Palmer, Tom Roberts, Pavel Snopok, Diktys Stratakis, and Alvin Tollestrup for help.

REFERENCES

- [1] M. Bogomilov *et al.*, *JINST*, vol. 7, p. 05009, 2012.
- [2] D. Adams *et al.*, *Eur. Phys. J.*, vol. C73, p. 2582, 2013.
- [3] D. Adams *et al.*, *JINST*, vol. 10, p. 12012, 2016.
- [4] L. Cremaldi *et al.*, *IEEE Trans. Nucl. Sci.*, vol. 56, p. 1475, 2009.

- [5] M. Bogomilov *et al.*, *JINST*, vol. 11, p. 03001, 2016.
- [6] S. Ozaki *et al.*, BNL-52623, 2001.
- [7] D. Neuffer, arXiv:1312.1266.
- [8] D. Stratakis and R. Palmer, *PRSTAB*, vol. 18, p. 031003, 2015.
- [9] C. Yoshikawa *et al.*, in *Proc. IPAC 2014*, paper TUPME016.
- [10] J. Gallardo *et al.*, Snowmass 1996, BNL, p. 52503.
- [11] D. Neuffer, Fermilab-FN-0319, 1979.
- [12] R. Palmer *et al.*, *AIP Conf. Proc.*, vol. 372, p. 31996.
- [13] R. Palmer *et al.*, *Nucl. Phys. Proc. Suppl.*, vol. 51A, p. 61, 1996.
- [14] C. M. Ankenbrandt *et al.*, *PRSTAB*, vol. 2, p. 081001, 1999.
- [15] M. M. Alsharo'a *et al.*, *PRSTAB*, vol. 6, p. 081001, 2003.
- [16] R. Palmer *et al.*, *PRSTAB*, vol. 8, p. 061003, 2005.
- [17] D. J. Summers *et al.*, in *Proc. PAC07*, paper THPMS082.
- [18] M. Chung *et al.*, *Phys. Rev. Lett.*, vol. 111, p. 184802, 2013.
- [19] B. Freemire, *et al.*, *Phys. Rev. Accel. Beams*, vol. 19, p. 062004, 2016.
- [20] D. V. Neuffer, *et al.* in *Proc. NAPAC -2016*, paper TUPOB06.
- [21] Y. Bao *et al.*, *Phys. Rev. Accel. Beams*, vol. 19, p. 031001, 2016.
- [22] R. B. Palmer, *et al.*, in *PAC 2007*, arXiv:0711.4275.
- [23] S. Feher and J. Strait, Snowmass -1996-ACC042.
- [24] D. J. Summers *et al.*, in *Proc. IPAC 2015*, paper TUPWI044.
- [25] C. Johnstone, M. Berz, D. Errede, and K. Makino, Fig. 5 on page 479, *Nucl. Instrum. Meth.*, vol. A519, p. 472, 2004.
- [26] Al Garren and Harold Kirk, MAP-DOC-4408, 2002.
- [27] H. Kirk *et al.*, in *Conf. Proc.* C030512, p. 2008, 2003.
- [28] A. Garren *et al.*, *AIP Conf. Proc.* vol. 821, p. 432, 2006.
- [29] F. Borgnolutti *et al.*, *IEEE Trans. Appl. Supercond.* vol. 24, p. 4003005, 2014.
- [30] P. Ferracin *et al.*, *IEEE Trans. Appl. Supercond.*, vol. 24, p. 4002306, 2014.
- [31] Hans Grote *et al.*, "MAD-X Methodical Accelerator Design Version 5.02.08 User's Reference Manual," 2016.
- [32] W. Herr and F. Schmidt, CERN-AB-2004-027-ABP.
- [33] E. D. Courant and H. S. Snyder, *Annals Phys.*, vol. 3, p. 1, 1958.
- [34] D. Neuffer, *Part. Accel.*, vol. 14, p. 75, 1983.
- [35] T. J. Roberts *et al.*, *Conf. Proc.* C0806233, paper WEPP120 2008.
- [36] R. C. Fernow, *eConf*, vol. C990329, paper THP31, 1999.
- [37] D. J. Summers *et al.*, arXiv:1504.03972.
- [38] J. G. Acosta *et al.*, in *Proc. COOL 2015*, paper MOPF07.
- [39] S. J. Oliveros *et al.*, presented at *NAPAC 2016*, paper MOB3CO04, this conference.
- [40] D. Neuffer, *AIP Conf. Proc.*, vol. 441, p. 270, 1998.